Chemical Science

ROYAL SOCIETY OF CHEMISTRY

EDGE ARTICLE

View Article Online
View Journal | View Issue

Cite this: *Chem. Sci.*, 2024, **15**, 16259

All publication charges for this article have been paid for by the Royal Society of Chemistry

A triazole-based covalent organic framework as a photocatalyst toward visible-light-driven CO_2 reduction to CH_4†

Sandip Biswas, [a] Faruk Ahamed Rahimi, [a] R. Kamal Saravanan,[a] Anupam Dey, [a] Jatin Chauhan,[a] Devika Surendran,[a] Sukhendu Nath [bc] and Tapas Kumar Maji *[a]

Solar-light driven reduction of CO_2 to CH_4 is a complex process involving multiple electron and proton transfer processes with various intermediates. Therefore, achieving high CH_4 activity and selectivity remains a significant challenge. Covalent organic frameworks (COFs) represent an emerging class of photoactive semiconductors with molecular level structural tunability, modular band gaps, and high charge carrier generation and transport within the network. Here, we developed a new heterocyclic triazole ring containing COF, **TFPB-TRZ**, through the condensation reaction between 1,3,5-tris(4-formylphenyl)benzene (TFPB) and 3,5-diamino-1,2,4-triazole (TRZ). The **TFPB-TRZ** COF with multiple heteroatoms shows suitable visible light absorption, high CO_2 uptake capability and an appropriate band diagram for CO_2 photoreduction. Photocatalysis results reveal a maximum CO_2 to CH_4 conversion of 2.34 mmol g^{-1} with a rate of 128 μmol g^{-1} h^{-1} and high selectivity (~99%) using 1-benzyl-1,4-dihydronicotinamide (BNAH) and triethylamine (TEA) as sacrificial agents. Under similar reaction conditions in the presence of direct sunlight, the **TFPB-TRZ** COF displays a maximum CH_4 yield of 493 μmol g^{-1} with a rate of 61.62 μmol g^{-1} h^{-1}, suggesting the robustness and light-harvesting ability of the COF photocatalyst. A femtosecond transient absorption (TA) spectroscopy study shows fast decay of excited state absorption (ESA) in the COF compared to the TFPB building unit due to efficient electron transfer to the catalytic site in the framework. The mechanism of CO_2 reduction to CH_4 is studied by DFT-based theoretical calculation, which is further supported by an *in situ* diffuse reflectance infrared Fourier transform spectroscopic (DRIFTS) study. The DFT results reveal that the lone pair of electrons on nitrogen heteroatoms present in the triazole ring of the TRZ moiety help in the stabilization of the CO intermediate during CO_2 to CH_4 conversion. Overall, this work demonstrates the use of a metal-free, recyclable COF-based photocatalytic system for solar energy storage by CO_2 reduction.

Received 14th May 2024
Accepted 4th September 2024

DOI: 10.1039/d4sc03163f

rsc.li/chemical-science

Introduction

Global industrialization and urbanization inevitably led to the excessive use of fossil fuels and the concomitant emission of greenhouse gases (mainly CO_2) into the earth's atmosphere.[1–5] Consequently, the replacement of traditional fossil fuel with renewable and clean energy has now become the utmost requirement to mitigate the energy and environmental crisis.[6–8] Numerous strategies towards carbon neutralization technologies have already been developed. Among them, converting CO_2 into energy fuels (such as CO, CH_4, CH_3OH and other C2 products) utilizing inexhaustible solar energy has been regarded as one of the finest and environmentally benign strategies for achieving the virtuous carbon cycle in nature.[7–11] However, we need to develop active photocatalysts to realize selective and efficient solar fuel production based on CO_2 photoreduction. A range of inorganic semiconductors, such as TiO_2,[12] WO_3,[13] Bi_2WO_6,[14] CdS,[15] ZrO_2,[16] In_2O_3,[17] $ZnGa_2O_4$,[18] as well as metal chalcogenides[19] and other carbonaceous materials have been investigated as photocatalysts for CO_2 reduction. However, most of them have drawbacks related to visible light absorption, relatively large band gap, poor mass transfer, binding of the reactant on the catalyst surface, and finally, environment friendliness.[20]

Metal–organic frameworks (MOFs) and covalent organic frameworks (COFs) are two widely explored crystalline porous materials with modular porosity and a porous environment.[21–29] The functionalities and application of these porous materials can be manipulated by design and customization of the

[a]*Molecular Materials Laboratory, Chemistry and Physics of Materials Unit, School of Advanced Materials (SAMat), Jawaharlal Nehru Centre for Advanced Scientific Research, Jakkur, Bangalore 560064, India. E-mail: tmaji@jncasr.ac.in; Web: https://www.jncasr.ac.in/faculty/tmaji*

[b]*Radiation and Photochemistry Division, Bhabha Atomic Research Center, Mumbai 400085, India*

[c]*Homi Bhabha National Institute, Mumbai 400094, India*

† Electronic supplementary information (ESI) available. See DOI: https://doi.org/10.1039/d4sc03163f

chemical nature, size and shape of the organic building units.[21–29] Suitable electronic band structures and visible light-absorption ability make them promising CO_2 photoreduction catalysts.[23,26] To date MOFs have been well studied in the field of photocatalysis, whereas metal-free organic porous materials like COF or conjugated microporous polymers are underexplored in the field of photocatalytic CO_2 reduction.[30,31] COFs have several advantages in terms of structural tunability, suitable band gap engineering, visible-light harvesting, and thermo-chemical stability.[20–23] Extended conjugation in the COF structure widens the scope of visible light absorption and facile charge transfer to the catalytic site.[32–45]

In spite of possessing the aforementioned advantages, CO_2 photoreduction using a metal-free COF as a catalyst is only limited to CO ($E_0 = -0.53$ V *vs.* NHE) or HCOOH ($E_0 = -0.61$ V *vs.* NHE).[9,40–45] However, using a COF as a photocatalyst for higher order CO_2 reduction products like CH_4 ($E_0 = -0.24$ V *vs.* NHE), which is considered the basic fuel of modern energetics, is yet to be reported. The redox potential of the photoexcited electrons, their reaction kinetics, binding energy and stabilization of different intermediates play a significant role in achieving a higher order multielectron CO_2 reduction process to CH_4. During the course of the reaction, such complexities can be controlled and fine-tuned *via* a suitable choice of building units for the COF structure. Since stabilization of the CO intermediate is the main hurdle for a higher order multielectron CO_2 reduction process, in metal-free catalysis, one way of stabilizing it is to involve the facile electron donation from a neighbouring group and satiating the π-accepting properties of CO species.[8] In this context, the incorporation of a small organic building unit like triazole with multiple heteroatoms into the framework may fulfil the purpose. The lone pair of electrons on nitrogen atoms present in triazole can provide a good electron-donating site for CO intermediate stabilization. Moreover, it is well known that triazole can have two tautomers, 1-H-triazole and 4-H-triazole, in between; the former is more stable.[46–48] Most importantly, the 1-H form of triazole, when present in the framework, will have a suitable arrangement of the lone pair-containing nitrogen atoms, which can stabilize the intermediate CO species (Scheme 1). Additionally, the overall electron density in the triazole component decorated with multiple heteroatoms in the COF would be high, which will further assist in multielectron CO_2 reduction beyond CO.

Keeping these attributes in mind herein, we have synthesized a new COF material through the general solvothermal Schiff base condensation between 1,3,5-tris(4-formylphenyl) benzene (TFPB) and 3,5-diamino-1,2,4-triazole (TRZ) with C3–C2 symmetrical topology, denoted as **TFPB-TRZ** (Scheme 1). Here, the TFPB moiety helps in bringing the extended π-conjugation into the backbone. The successful formation of the COF was confirmed by various characterization methods, including powder X-ray diffraction (PXRD), FT-IR, ^{13}C CP-MAS NMR and N_2 sorption measurements. The as-synthesized **TFPB-TRZ** COF was successfully implemented as a metal-free

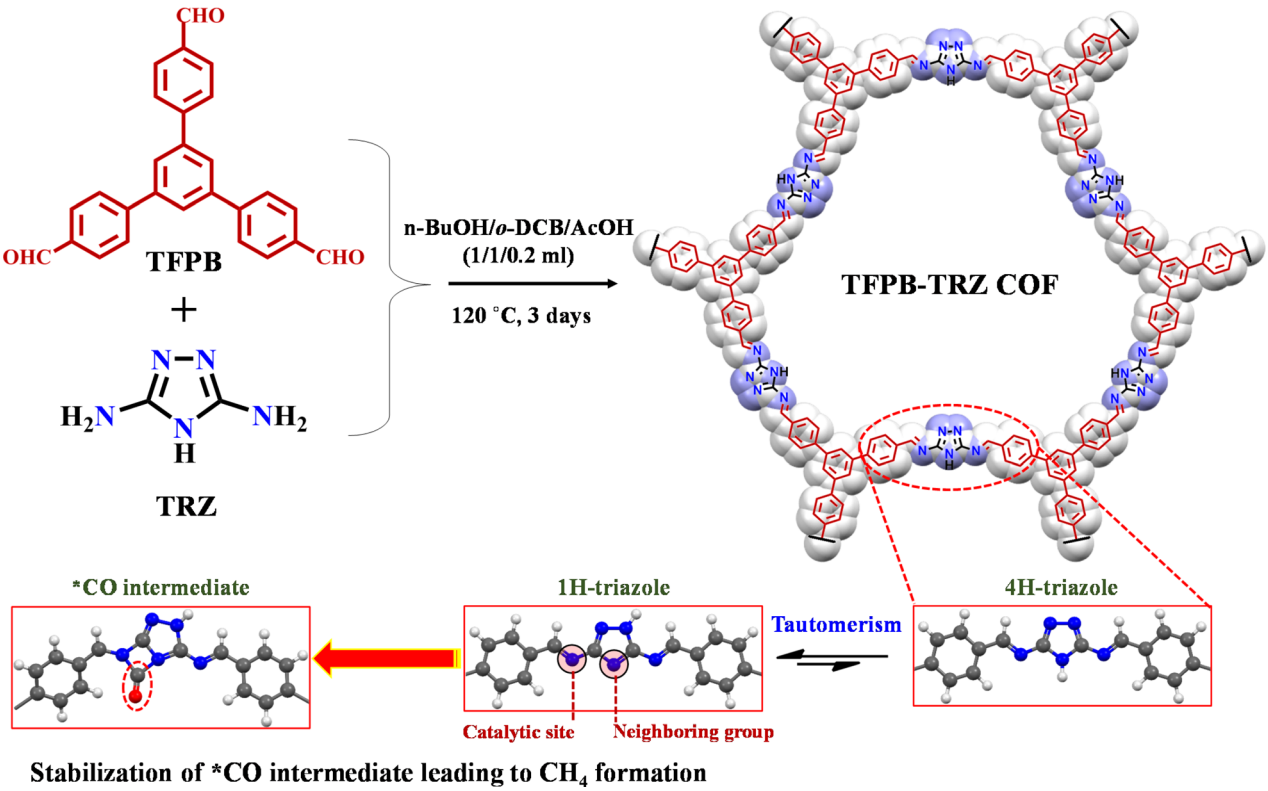

Scheme 1 A synthetic scheme for the TFPB-TRZ COF based on a Schiff-base condensation reaction. Top view of the TFPB-TRZ COF. Bottom panel: tautomerism in 1,2,4-triazole. Schematic of the stabilization of *CO intermediate during CO_2 reduction by the nitrogen heteroatom of the 1H-triazole form. Color code: H, white; C, grey; N, blue; O, red.

heterogeneous photocatalyst for visible-light-driven CO_2 reduction to CH_4 with excellent yield (2.34 mmol g^{-1} in 18 h) and high selectivity (~99%) in the presence of sacrificial agents. Catalytic activity is further explored under direct sunlight, where it produces ~493 μmol g^{-1} of CH_4 after 8 h of reaction. The electron transfer kinetics in the COF for eight electron CO_2 reduction to CH_4 was further supported by the transient absorption (TA) spectroscopic study.[43,49–51] Crucial information on the reaction intermediates during the conversion of CO_2 to CH_4 has been obtained through an *in situ* diffuse reflectance infrared Fourier-transform (DRIFT) study along with the free energy calculation that supported the thermodynamic feasibility of the formation of different intermediates. The formation of CH_4 by a COF-based metal-free photocatalyst provides a new avenue for the rational design of porous crystalline materials for multielectron photoreduction.

Results and discussion

The TFPB precursor was synthesized according to the previous report and characterized using ^{1}H NMR spectroscopy (Fig. S1†). After several trial-and-error attempts by varying the reaction conditions (Table S1 and Fig. S2†), the **TFPB-TRZ** COF was synthesized solvothermally by reacting a 3 : 2 mixture of TFPB and TRZ precursors using a 1 : 1 mixture of *ortho*-dichlorobenzene (*o*-DCB) and *n*-butanol in a high-precision glass tube, which was flame sealed and kept at 120 °C for three days in the presence of 6 M acetic acid (Scheme 1). The product was first characterized by a powder X-ray diffraction (PXRD) technique (Fig. 1a). The structure of the COF was modelled both in eclipsed (AA) (Fig. 1c) and staggered (AB) stacking arrangements (Fig. 1e) and compared with the experimental data. The Pawley refinement using AA stacking was found to be well-matched with the experimental data in terms of intensity ratios with an acceptable difference ($R_{wp} = 1.75\%$, $R_p = 1.37\%$; Fig. 1a). The AB stacking model did not replicate the experimentally obtained data. A typical trigonal lattice with the *P*31*m* space group was obtained with the unit cell parameters of $a = b = 35.60$ Å, $c = 3.49$ Å, $\alpha = \beta = 90°$, $\gamma = 120°$. The PXRD pattern of the **TFPB-TRZ** COF showed six prominent diffraction peaks, with the most intense one at 2.88° indicating the presence of the (100) crystal plane of the **TFPB-TRZ** COF (Fig. 1a). Additionally, the other relatively weak diffractions at 4.9°, 7.4°, 10.3°, 12.6° and 25.9° indicated the existence of (110), (210), (310), (320) and (001) facets, respectively (Fig. 1a). The peak at $2\theta = 25.9°$ (001 plane)

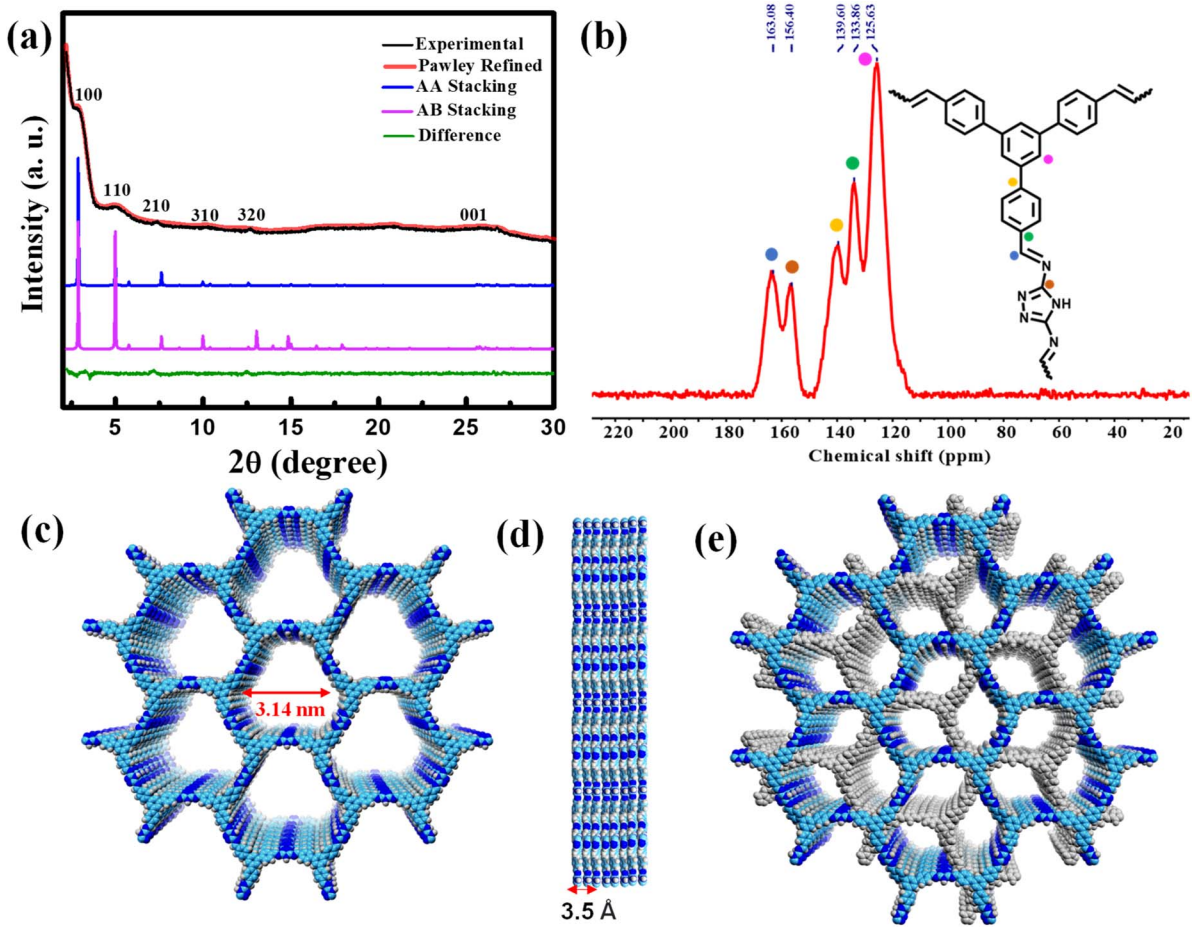

Fig. 1 (a) Comparison between the experimental and theoretical PXRD patterns. Pawley refinement (red) showing good fit (AA stacking) to the experimental data (black) with minimal differences (olive). (b) Solid-state ^{13}C CP-MAS NMR spectrum of the **TFPB-TRZ** COF. (c and e) Possible eclipsed and staggered conformations of the **TFPB-TRZ** COF. (d) Stacking distance between the two adjacent layers.

was possibly due to the interlayer stacking of the COF, and distances between the individual (001) planes were 3.43 Å.

The chemical constitution of the obtained **TFPB-TRZ** COF was further analyzed using Fourier transform infrared (FT-IR) and ^{13}C cross-polarization/magic angle spinning solid-state nuclear magnetic resonance (CP/MAS ssNMR) spectroscopy (Fig. S3a† and 1b). The FTIR spectrum of the **TFPB-TRZ** COF showed a band at 1690 cm^{-1} corresponding to –C═N– stretching and also the disappearance of –N–H stretching bands of the TRZ monomer, supporting the formation of the COF by a Schiff base condensation reaction (Fig. S3a†). The peak at 163 ppm in the solid-state ^{13}C NMR spectrum of the **TFPB-TRZ** COF was attributed to the –C═N– bonds in the COF (Fig. 1b). Signals around 120 to 140 ppm belong to the aromatic carbons (Fig. 1b). Thus, FT-IR and ^{13}C CP-MAS NMR provided unequivocal evidence of the successful condensation of the aldehyde and amine into an imine linked structure. Thermogravimetric analysis (TGA) under nitrogen was also employed to test the thermal stability of the **TFPB-TRZ** COF, which showed that the as-synthesized COF retained structural stability until 300 °C (Fig. S3b†). Since no significant weight loss was observed before the onset of decomposition, it can be concluded that the framework was virtually free of trapped guest molecules (Fig. S3b†).

The scanning electron microscopy (SEM) image revealed the short fibrous morphology of the **TFPB-TRZ** COF (Fig. 2a). Homogeneous distribution of C and N throughout the entire framework was seen from the SEM elemental mapping (Fig. S4†). A transmission electron microscopy (TEM) image confirmed the fibrous morphology of the crystalline framework (Fig. 2b). The high-resolution transmission electron microscopy (HR-TEM) image revealed a lattice spacing of 3.4 Å, which can be attributed to the regular arrangement of the 2D network (Fig. 2c). The selected area electron diffraction (SAED) pattern additionally confirmed the highly crystalline nature of the COF (inset, Fig. 2c). Atomic force microscopy (AFM) imaging confirmed the fibrous morphology, and height profile analysis suggested that the height and width were within the range of 15 ± 0.5 nm and 100 ± 10 nm, respectively (Fig. 2d).

The porosity of the **TFPB-TRZ** COF was examined by N_2 adsorption–desorption measurement at 77 K and showed a type II adsorption isotherm, unveiling the micro and mesoporous characteristics of the COF (Fig. 2e). The Brunauer–Emmett–Teller (BET) surface area of the **TFPB-TRZ** COF was determined to be 385 $m^2 g^{-1}$. The wide pore size distribution obtained from the non-linear density functional theory (NLDFT) calculation can be attributed to the inherent porosity and fibrous morphology of the COF (Fig. S5†). Furthermore, CO_2 (kinetic

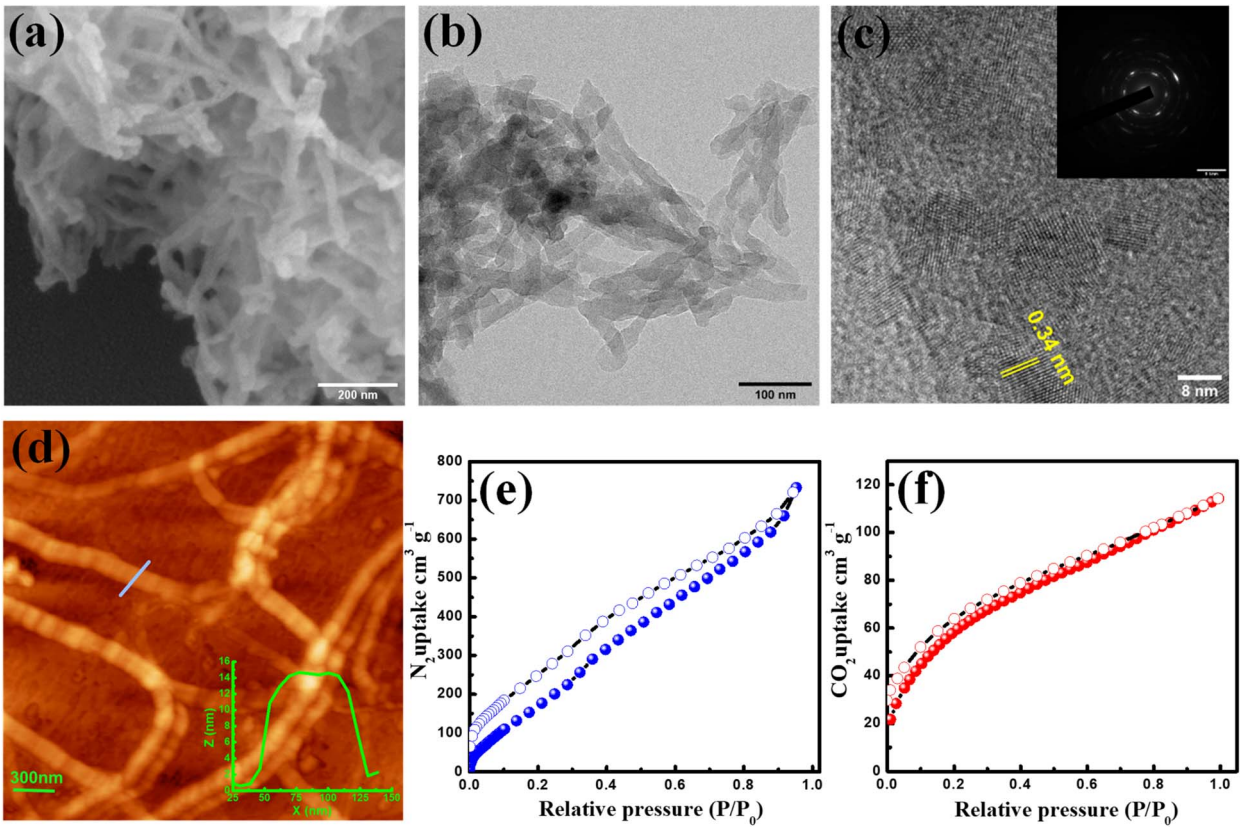

Fig. 2 (a) SEM image of the TFPB-TRZ COF showing fibrous morphology. (b) TEM image of the TFPB-TRZ COF showing entangled fiber like morphology. (c) HR-TEM image exhibiting lattice fringes with an interplanar distance of 0.34 nm. Inset shows the corresponding SAED pattern. (d) Tapping mode AFM images of the COF showing the fibers. Inset: height profile analysis suggests that the height and width of the tubes are within the range of 15 ± 0.5 nm and 100 ± 10 nm. (e) N_2 adsorption isotherm for the TFPB-TRZ COF measured at 77 K. (f) CO_2 adsorption isotherm measured at 195 K.

diameter 3.3 Å) adsorption measurement was performed at 195 K for the **TFPB-TRZ** COF exhibiting a typical type-I profile with an uptake amount of 120 $cm^3\ g^{-1}$ again suggesting the microporous nature of the framework (Fig. 2f).

UV-vis diffuse reflectance spectroscopy (DRS) and photoluminescence (PL) spectroscopy were used to study the photophysical properties of the COF (Fig. 3a and b). The **TFPB-TRZ** COF exhibited a broad visible light absorption with a maximum of around 440 nm. In comparison to the **TFPB-TRZ** COF, the monomer TRZ showed an absorption maximum at ~300 nm and TFPB displayed a broad absorption in the range of ~350–500 nm (Fig. 3a). This suggested that the imine conjugated TFPB unit in the **TFPB-TRZ** COF is the main component for visible light absorption (Fig. 3a). To verify that, time-dependent density functional theory (TDDFT) calculation was performed on a TFPB-imine fragment, which revealed a band appearing at 453.24 nm due to the transition between the highest occupied molecular orbital (HOMO) and the lowest unoccupied molecular orbital (LUMO). The molecular orbital analysis further disclosed that the band at ~440 nm of the COF appeared due to the extended conjugation through imine bonds with the TFPB core (Fig. 3e and Table S2†). The calculated energy corresponding to the HOMO–LUMO transition is 2.74 eV, which is in close agreement with the experimentally determined optical band gap of 2.55 eV obtained from the Tauc plot (inset, Fig. 3a). The solid phase PL spectrum of the **TFPB-TRZ** COF showed a significantly red-shifted emission (λ_{max} = 530 nm, λ_{ex} = 410 nm) compared to its corresponding monomers TFPB (λ_{max} = 405 nm, λ_{ex} = 350 nm) and TRZ (λ_{max} = 445 nm, λ_{ex} = 290 nm) which can be attributed to the extended π-conjugation in the COF skeleton (Fig. 3b).[43,50,52] Time-correlated single-photon counting (TCSPC) measurement revealed a relatively shorter average lifetime of ~0.88 ns for the **TFPB-TRZ** COF in comparison to the average lifetime of 1.92 ns for the TFPB building block (Fig. S6 and Table S3†).

Furthermore, Mott–Schottky (MS) measurements were conducted on the **TFPB-TRZ** COF at a frequency of 500, 1000, 1500, and 2000 Hz at pH 7 in a 0.2 M Na_2SO_4 electrolyte to determine the conduction-band (CB) position (Fig. 3c). The CB position was estimated to be −0.61 V *vs.* normal hydrogen electrode (NHE), which is more negative than the reduction potential of CO_2 to CO/CH_4 (−0.53/−0.24 V *vs.* NHE at pH 7) (Fig. 3c). The valence band (VB) position is 1.94 V as obtained from the band gap and CB position (Fig. 3d). A schematic representation of the band diagram towards a feasible CO_2 reduction process is presented in Fig. 3d. Furthermore, volumetric CO_2 adsorption measurements were conducted on the activated sample at 298 K as well as at 273 K, and the CO_2 uptake amounts were found to be ~12 and ~18 $cm^3\ g^{-1}$ (Fig. 3f). The isosteric heat of adsorption of the COF is about 22.5 kJ mol^{-1}, indicating that the **TFPB-TRZ** COF has a good affinity toward CO_2 (Fig. S7†).

The **TFPB-TRZ** COF was tested as the photocatalyst for the photoreduction of CO_2 under different conditions under xenon lamp irradiation (800 > λ > 400 nm, 300 W xenon lamp). The photo-reduced gaseous products were analyzed and quantified by gas chromatography-mass spectrometry (GC-MS) analysis

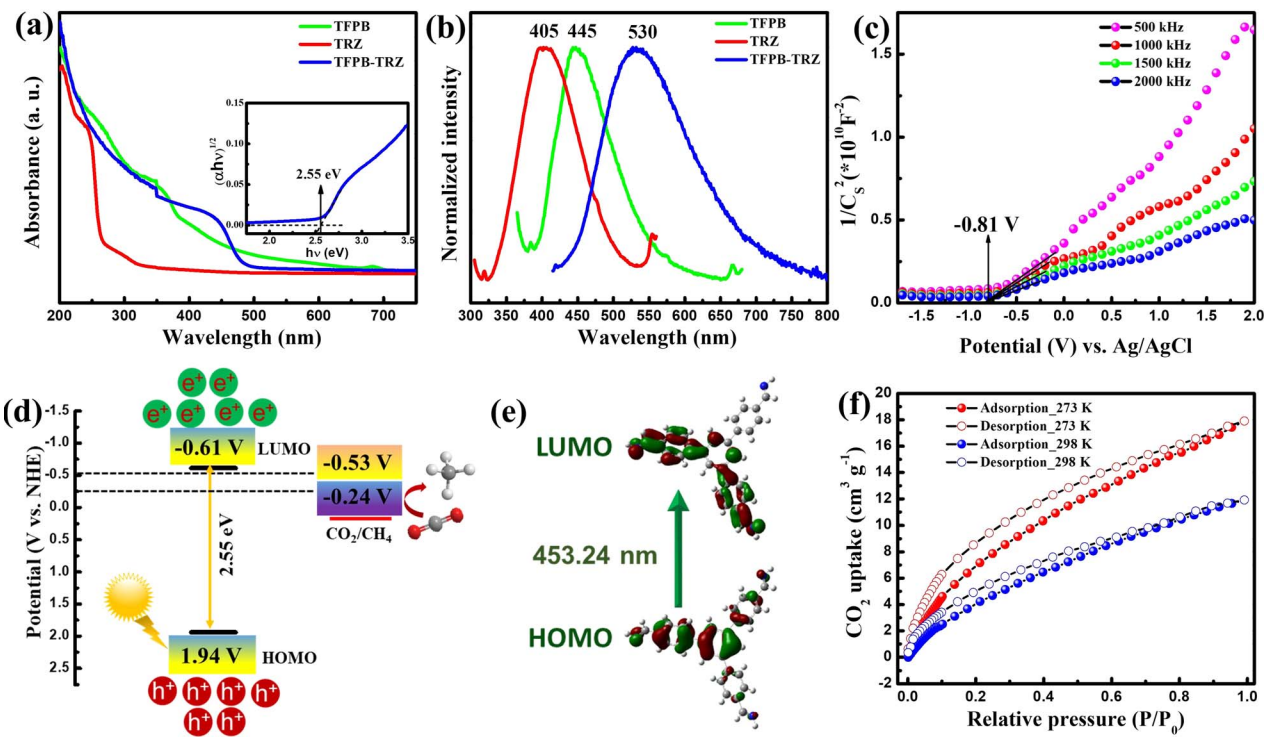

Fig. 3 (a) Diffuse reflectance UV-visible spectra (inset: band gap of the **TFPB-TRZ** COF determined by the Tauc plot) and (b) emission spectra of the **TFPB-TRZ** COF, TFPB and TRZ monomers. (c) Mott–Schottky plot of the **TFPB-TRZ** COF showing the flat band potential using the conventional three electrode system in a 0.2 M Na_2SO_4 solution. (d) Band diagram for the **TFPB-TRZ** COF based on the Mott–Schottky analysis and optical band gap measurement (in the NHE scale at pH 7). (e) Frontier molecular orbitals of the repeating unit of the **TFPB-TRZ** COF based on TDDFT calculation using the 6-31+G** basis set in the B3LYP-D3 method. (f) CO_2 adsorption isotherms at 273 K (red) and 298 K (blue).

from the head-space of the reactor every two hours. At first, we explored the catalytic activity of the **TFPB-TRZ** COF in a pure aqueous medium without any sacrificial agent (Fig. S10a†). After 18 h of reaction, 140 μmol g^{-1} of CH_4 and ~10 μmol g^{-1} of CO were formed in pure water medium (Fig. S8, S9 and S10a†). Then, we investigated the photocatalytic activity in an acetonitrile (ACN)–water (H_2O) (2 : 1) mixed solvent system using only triethylamine (TEA) as the sacrificial electron donor where 190 μmol g^{-1} of CH_4 and ~20 μmol g^{-1} of CO were evolved after 18 h of photocatalysis (Fig. S10b†). Afterwards, the photocatalytic CO_2 reduction performance of **TFPB-TRZ** was checked in aqueous medium using the combination of 1-benzyl-1,4-dihydronicotinamide (BNAH) and TEA as sacrificial agents (Fig. S10c†). As shown in Fig. S10c,† ~331 μmol g^{-1} of CH_4 and ~15 μmol g^{-1} of CO were formed after 18 h of reaction. Finally, in an ACN–H_2O (2 : 1) mixed solvent system using BNAH and TEA as sacrificial agents, a significant amount of CH_4 (~2304 μmol g^{-1}) and a negligible amount of CO (~194 μmol g^{-1}) and H_2 (~40 μmol g^{-1}) were produced in 18 h (Fig. 4a). However, no liquid product was formed in the course of photocatalysis, as confirmed by the ^1H NMR study (Fig. S11†). The production rate and selectivity of CH_4 formation were found to be 128 μmol g^{-1} h^{-1} and ~99%, respectively. To the best of our knowledge, this is the first report on visible light-driven $8e^-$ reduction of CO_2 to CH_4 by a COF (Table S4†). Interestingly, when the photocatalytic experiment was performed using only BNAH as a sacrificial agent in the mixed solvent system, the catalytic activity was not significant (CO: 7.0 μmol g^{-1}; CH_4: 50.0 μmol g^{-1} in 18 h) (Fig. S12†). Several other control experiments were performed in the dark, under an N_2 atmosphere and without the catalyst, in which no CO_2 reduction product was found, indicating the profound role of the **TFPB-TRZ** catalyst towards successful photocatalytic CO_2 reduction (Fig. S13†). The enhanced catalytic efficiency in the presence of both BNAH and TEA can be attributed to the following reasons. First, BNAH (E^0_{ox} = 0.57 V *vs.* SCE) is a stronger reducing agent compared to TEA (E^0_{ox} = 0.69 V *vs.* SCE). As a result, BNAH is easier to oxidize than the other sacrificial electron donors, which helps in faster quenching of the hole during photocatalysis under visible light irradiation. Secondly, one-electron oxidation of BNAH induces deprotonation to yield BNA˙ which can easily dimerize to form BNA_2 and its reduction power (E^0_{ox} = 0.26 V *vs.* SCE) is stronger than that of BNAH, enabling faster reductive quenching of the excitons.[8,9,53–56] Additionally, due to the better solubility of CO_2, the sacrificial agents in ACN medium propelled faster diffusion of the CO_2 to the catalytic site of the COF, leading towards enhanced catalytic activity. To mimic the natural photosynthesis process, we next verified the **TFPB-TRZ** COF catalyzed CO_2 reduction in the mixed solvent system using BNAH and TEA under direct sunlight between 9:00 am and 5:00 pm for five days from 15th to 19th July 2022 (Fig. 4b). On the sunniest day of 19th July, ~493 μmol g^{-1} of CH_4 production upon 8 h (activity = 61.62 μmol g^{-1} h^{-1}) of sunlight irradiation was realized, suggesting the robustness and sunlight-harvesting ability of the **TFPB-TRZ** COF (Fig. 4b). The photocurrent response of the **TFPB-TRZ** COF was then conducted to understand the charge

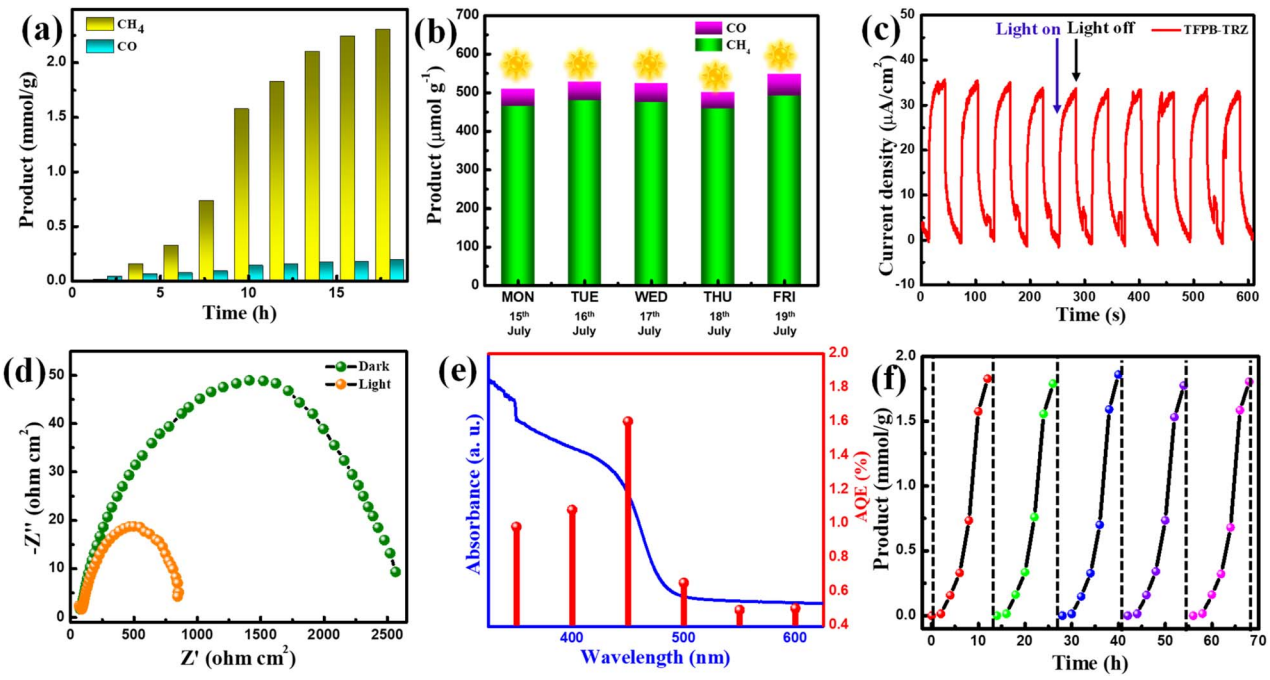

Fig. 4 (a) Time-dependent CO_2 reduction product formation in ACN–H_2O (2 : 1) medium in the presence of BNAH and TEA involving the **TFPB-TRZ** COF as the photocatalyst. (b) Sunlight-driven CO_2 reduction with the **TFPB-TRZ** COF in ACN–H_2O mixture for 8 h. (c) Transient photocurrent response of the **TFPB-TRZ** COF in 0.2 M Na_2SO_4 aqueous solution under visible-light irradiation. (d) Electrochemical impedance spectra (Nyquist plot) of the **TFPB-TRZ** COF showing the charge transfer resistance under light (orange) and in the dark (green). (e) AQE of the CO_2RR for the **TFPB-TRZ** COF at different wavelengths of monochromatic light under irradiation for 6 h. (f) Recyclability plot of CH_4 production during 12 h of photocatalysis for each run.

separation by light irradiation (Fig. 4c). The generation of high photocurrent (35 μA cm^{-2}) further supports the efficient charge separation ability of the COF under light irradiation (Fig. 4c). The charge transfer ability of the **TFPB-TRZ** COF was further validated by an electrochemical impedance spectroscopy (EIS) study under both light and dark conditions (Fig. 4d). The semicircle radius in the Nyquist plot decreased significantly in the presence of light, which indicates much better charge transfer under light irradiated conditions in comparison to the dark, benefitting the photocatalytic activity (Fig. 4d). Apparent quantum efficiencies (AQEs) for the **TFPB-TRZ** photocatalyst were measured under various wavelengths and were found in parallel agreement with the HOMO–LUMO band gap of the TFPB-imine fragment (Fig. 4e). The **TFPB-TRZ** COF manifested a maximum AQE value of 1.6% under monochromatic light irradiation of 450 nm (see the ESI† for more details). Next, the recyclability of the **TFPB-TRZ** photocatalyst was evaluated for up to five consecutive cycles under a mixed solvent system in the presence of BNAH and TEA (Fig. 4f). After each catalytic cycle, the catalyst was recovered from the reaction mixture and again utilized for the next cycle under similar conditions, which showed no significant change in the yield for five consecutive cycles, hence suggesting the durability and reusability of the COF as a photocatalyst (Fig. 4f). An isotope labeling experiment was performed with $^{13}CO_2$, which produced $^{13}CH_4$, which unambiguously confirmed that the origin of CH_4 is from the reduction of CO_2 (Fig. S14†). Other than the decrease in the intensity ratios, no obvious change was seen in the PXRD pattern of the post-catalytic sample in comparison to the pristine COF, indicating the robustness of the COF structure (Fig. S15†). FT-IR and TEM analysis of the recovered sample further supports the molecular connectivity, and the structure of the COF skeleton remained intact after photocatalysis (Fig. S16†).

Femtosecond transient absorption (TA) experiments were performed to further confirm the electron transfer from the TFPB moiety to the catalytic site in the COF. The TA absorption spectra of TFPB in acetonitrile solution showed an excited state absorption (ESA) band peaking at ~525 nm with a tailing broad absorption extending beyond 700 nm (Fig. 5a). The decay trace recorded at 525 nm was characterized by two growth

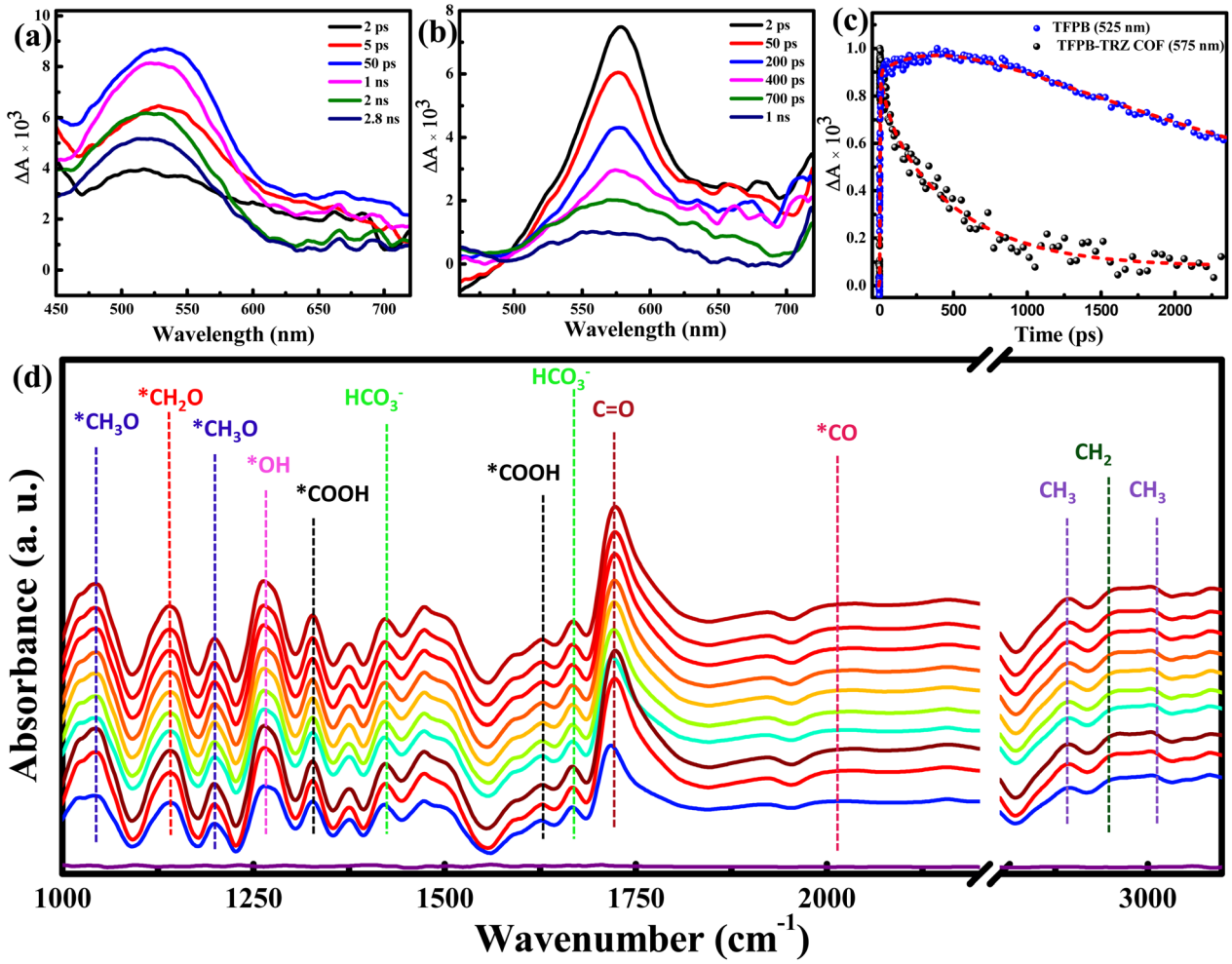

Fig. 5 Transient absorption spectra of (a) TFPB and (b) **TFPB-TRZ** COF at different time delays between the pump and probe pulse. (c) Decay kinetics for TFPB (525 nm) and **TFPB-TRZ** COF (575 nm). The dashed curves show the fitting of the experimental data. (d) *In situ* DRIFT measurement for photocatalytic CO_2 reduction using the **TFPB-TRZ** COF as a catalyst in the presence of CO_2, BNAH, TEA, and H_2O vapor under visible light irradiation (LED lamp, $\lambda > 400$ nm).

components of 2.6 ps and 280 ps (Fig. 5c). Considering the polar nature of the solvent, the faster growth component of 2.6 ps was assigned due to the solvent relaxation process in the excited state of TFPB. Since TFPB consists of three 4-formylphenyl groups connected to the central benzene moiety through single bonds, there was a high probability that the torsional motion of the 4-formylphenyl group around the single bond could take place in its excited state. Such excited state torsional motion is well known for molecular rotors.[57,58] Hence, the longer growth component of 280 ps was assigned to the excited state torsional dynamics in TFPB. Besides such a growth component, the ESA signal of TFPB showed a long decay time (>2 ns) which could not be determined accurately due to the limited temporal window of our measurements (2.5 ns). Such a long excited state decay time constant is also supported by the nanosecond decay component observed in the TRPL measurements (Fig. S6 and Table S3†). The transient absorption spectra of the **TFPB-TRZ** COF showed a red-shifted ESA band having maxima at ~575 nm (Fig. 5b). The red shift of ~50 nm in the ESA band was due to the introduction of extended π-conjugation between TFPB and TRZ in the COF.[59] However, unlike TFPB, no growth in the ESA band in the **TFPB-TRZ** COF was observed. This is expected due to the formation of a large and closed chemical network between TFPB and TRZ. The formation of such a network completely suppressed the torsional dynamics in the excited state.[51] The fitting of the ESA signal of the **TFPB-TRZ** COF results in the decay time constants of 55 ps (18%) and 510 ps (76%) along with a low amplitude (6%) residual signal which can have a longer decay time constant compared to our temporal window of TA setup. This residual signal is mainly responsible for the longer decay observed in the TRPL measurements of the **TFPB-TRZ** COF (Fig. S6 and Table S3†). The faster decay time constant observed in the **TFPB-TRZ** COF than in TFPB is mainly due to the electron transfer from TFPB to the catalytic site. Thus, the transient absorption data further support the faster transport of charge carriers in the **TFPB-TRZ** COF, resulting in higher ordered CO_2 reduction products.

We have performed an *in situ* diffuse reflectance infrared Fourier transform (DRIFT) spectroscopic study to probe reaction intermediates during photocatalytic CO_2 reduction to CH_4 associated with the **TFPB-TRZ** COF photocatalyst in a mixed solvent system using BNAH and TEA as sacrificial electron donors (Fig. 5d). Peaks appearing at 1421 and 1666 cm^{-1} were ascribed to the symmetric and asymmetric stretching of HCO_3^-, respectively.[8,60] Peaks at 1325 and 1625 cm^{-1} corresponded to a *COOH species, which is a crucial intermediate during the photochemical conversion of CO_2 to CH_4 or CO.[8,9,60,61] Notably, stretching vibration for the *CO intermediate was observed at 2010 cm^{-1}. The peak observed at 1724 cm^{-1} is attributed to the stretching vibration of aldehyde C=O.[62] The presence of the $*CH_2O$ intermediate was supported by the band at 1140 cm^{-1}.[63] The observation of new IR peaks at 1043 and 1200 cm^{-1} was attributed to the $*CH_3O$ intermediate,[60] suggesting that $*CH_2O$ and $*CH_3O$ are intermediate species of CO_2 photoreduction to CH_4. In addition to that, the peak at 2947 cm^{-1} corresponds to the asymmetric (ν_{as}) stretching vibration of $-CH_2$.[8,9,61–63] Besides, peaks at 2890 and 3000 cm^{-1} were ascribed to the symmetric (ν_s) and asymmetric (ν_{as}) stretching vibrations of the $-CH_3$ intermediate, respectively.[8,9,61–63] Hence, the detection of the key intermediates clearly suggested the progress of the photochemical $8e^-$ reduction of CO_2 to CH_4.

Furthermore, density functional theory (DFT) calculations were performed to understand the underlying catalytic mechanism behind the photocatalytic conversion of CO_2 to CH_4 on the **TFPB-TRZ** COF catalyst (Fig. 6). The DFT calculations were performed with the guidance of earlier literature reports and the intermediates traced from the *in situ* DRIFT study.[8,9,52] For theoretical calculations, a small fragment of the **TFPB-TRZ** COF catalyst consisting of two TFPB and one TRZ unit was taken into consideration, which can be represented as TFPB-TRZ-TFPB (*). The photocatalytic process was initiated with one electron photoreduction of the initial catalyst TFPB-TRZ-TFPB (*), which formed the intermediate $[TFPB\text{-}TRZ\text{-}TFPB]^-$ ($*^-$) ($\Delta G = -0.93$ eV). Next, the reactant CO_2 was bound on the intermediate $[TFPB\text{-}TRZ\text{-}TFPB]^-$ ($*^-$), which was the most crucial step for CO_2 reduction catalysis. In order to identify the CO_2-binding site on $[TFPB\text{-}TRZ\text{-}TFPB]^-$ ($*^-$), we performed CO_2-binding energy calculation which revealed that the imine nitrogen was the most suitable active center for CO_2-binding during catalysis (Fig. S17†). The CO_2-binding to the intermediate $[TFPB\text{-}TRZ\text{-}TFPB]^-$ ($*^-$) resulted in the formation of the $*CO_2^-$ intermediate, which was a slightly uphill process ($\Delta G = +0.12$ eV) with an activation barrier of 0.48 eV. In the next step of the catalytic process, $*CO_2^-$ intermediate underwent protonation to generate the *COOH intermediate ($\Delta G = -0.40$ eV), which after photoreduction afforded the $*COOH^-$ intermediate ($\Delta G = -0.88$ eV). Next, the intermediate $*COOH^-$ after subsequent protonation and water elimination resulted in the formation of the *CO intermediate ($\Delta G = +1.54$ eV). In metal-free CO_2 reduction catalysis, the challenging aspect is to prevent the desorption of CO to achieve the higher-ordered CO_2 reduction product. Reportedly, the stabilization of the *CO intermediate on the metal-free catalyst can be achieved through additional electron donation to the adsorbed *CO by an electron-rich neighboring group.[8] Interestingly, DFT calculations revealed that the **TFPB-TRZ** COF catalyst is capable of doing that. The 1,2,4-triazole moiety present in this catalyst was reported to exist in rapid equilibrium between its two tautomeric forms, namely, 1H-triazole and 4H-triazole (Fig. 6b).[46–48] In the **TFPB-TRZ** COF catalyst, the TRZ in its 1H-triazole form was able to stabilize the *CO intermediate by donating electrons to the CO species (Fig. 6c and S18†). The presence of the mild base TEA during the catalysis can easily trigger the interconversion between the two tautomers (Fig. 6d). This could be verified by the experimental results of photocatalysis performed in the absence of the base TEA. The catalysis performed with only the BNAH sacrificial agent displayed poorer catalytic activity than the solely used TEA (Fig. S12†), which indicated that the basicity of the sacrificial agent also plays an important role along with the reductive quenching of the exciton. In the next step of the catalytic mechanism, the intermediate *CO would undergo proton-coupled reduction to form the *CHO intermediate ($\Delta G = -5.23$ eV) as the release of CO from the *CO intermediate was less feasible ($\Delta G = -3.66$ eV) (Fig. S18†), which justified the high

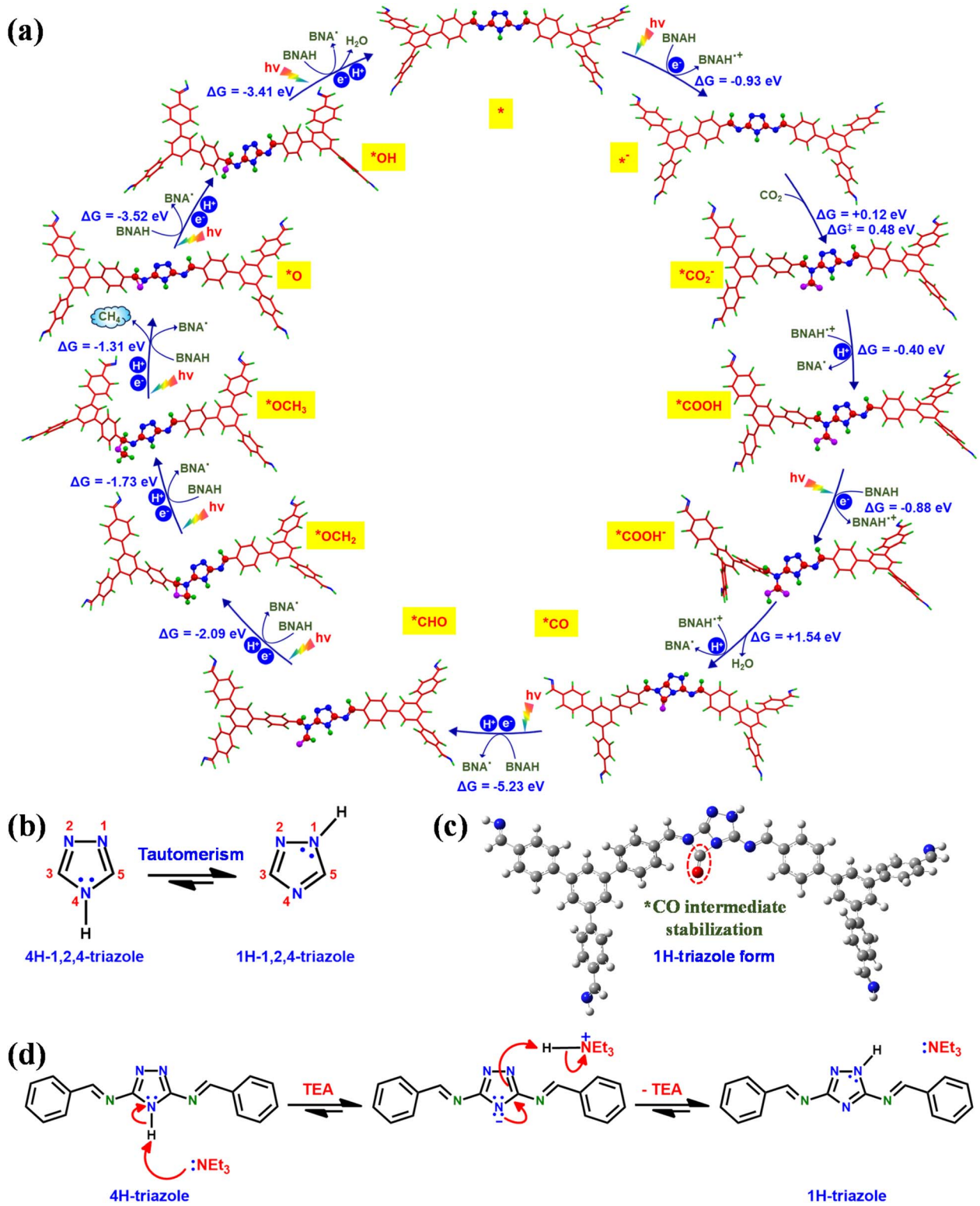

Fig. 6 (a) Possible mechanism for photocatalytic CO_2 reduction to CH_4 on the **TFPB-TRZ** COF catalyst. (b) Tautomerism in 1,2,4-triazole. (c) Stabilization of the *CO intermediate in the 1H-triazole form. (d) Dynamic equilibrium between the tautomers of the TRZ moiety in the presence of a mild base TEA.

selectivity of CH_4 production over CO during photocatalysis. The rapid conversion of the *CO intermediate could be easily perceived from its highly exergonic conversion steps, which is quite expected from the highly reactive *CO containing a strained four-member ring. In the following steps, successive proton-coupled reductions converted the *CHO intermediate to

*OCH_2 ($\Delta G = -2.09$ eV) to *OCH_3 ($\Delta G = -1.73$ eV). Further proton-coupled reduction of the *OCH_3 intermediate led to the generation of the *O intermediate[64] and CH_4 was produced in the process ($\Delta G = -1.31$ eV). After proton-coupled reduction, the *O intermediate converted to the *OH intermediate ($\Delta G = -3.52$ eV), which subsequently released water after another proton-coupled reduction to regenerate the initial catalyst [TFPB-TRZ-TFPB] (*) ($\Delta G = -3.41$ eV). Thus, the recovered initial catalyst TFPB-TRZ-TFPB (*) again entered into the catalytic process (Fig. 6a and S18†). An important point to be noted: in the whole catalytic process, the formation of the *CO intermediate was the most uphill process ($\Delta G = +1.54$ eV), which suggested that the rate-determining step of the photocatalytic process was the *CO formation step. Further details about the DFT calculations are presented in the ESI (Fig. S17, S18, and Tables S5–S30).†

Conclusions

In summary, we have demonstrated how photocatalytic CO_2 reduction can be manipulated *via* a suitable selection of monomer building unit in the COF material. Here, a **TFPB-TRZ** COF was synthesized through the solvothermal method, employing 1,3,5-tris(4-formylphenyl)benzene and 3,5-diamino-1,2,4-triazole monomer building units. The metal-free **TFPB-TRZ** COF displayed CO_2 to CH_4 conversion with an impressive rate and high selectivity (~99%) under visible-light irradiation. Furthermore, the **TFPB-TRZ** COF showed promising catalytic activity under direct sunlight irradiation, suggesting an efficient light-harvesting ability. Femtosecond transient absorption (TA) spectroscopy revealed the fast electron transfer kinetics in the COF compared to the TFPB monomer, facilitating the higher-order CO_2 photoreduction. *In situ* DRIFT analysis indicated the real-time reaction progress of the CO_2 to CH_4 photoreduction process. Theoretical studies based on these observations provided mechanistic insights of $8e^-$ reduction of CO_2 to CH_4 by the **TFPB-TRZ** COF photocatalyst. The nitrogen heteroatoms present in the triazole ring of TRZ help in the stabilization of the CO intermediate by electron donation, benefitting CO_2 to CH_4 conversion. In a nutshell, photocatalytic proficiency in CO_2 reduction to CH_4 in a COF-based system underscores the superiority and uniqueness and offers valuable perspectives for the design and synthesis of high-performance, cheap and robust metal-free photocatalysts.

Data availability

All the associated data are available in the ESI.†

Author contributions

S. B. and T. K. M. designed the concept of this work. S. B., K. S., A. D. and J. C. performed major experiments. S. B., F. A. R., and T. K. M. analyzed the experimental data and wrote the manuscript. F. A. R. conducted all the computational studies. A. D. and D. S. did simulation studies of PXRD patterns. All authors discussed the results and commented on the manuscript.

Conflicts of interest

There are no conflicts to declare.

Acknowledgements

All the authors acknowledge the support and resources provided by the "PARAM Yukti Facility" under the National Supercomputing Mission, Government of India, at JNCASR, Bangalore. S. B. acknowledges the Science and Engineering Research Board (SERB), Department of Science and Technology (DST) for the National Postdoctoral fellowship (NPDF). A. D. and F. A. R. thank the CSIR (Government of India) for a fellowship. Mr Soumya Kanti Mondal, CPMU, JNCASR is gratefully acknowledged for virial fitting of CO_2 adsorption isotherms at two different temperatures. T. K. M. acknowledges the Department of Science and Technology (Projects SPR/2021/000592), RAK-CAM (from UAE), SSL, ICMS, and JNCASR for financial support. The SAMat research facility and Sheikh Saqr senior fellowship are also gratefully acknowledged by T. K. M.

Notes and references

1 G. A. Olah, G. K. S. Prakash and A. Goeppert, Anthropogenic Chemical Carbon Cycle for a Sustainable Future, *J. Am. Chem. Soc.*, 2011, **133**, 12881–12898.
2 S. J. Davis, K. Caldeira and H. D. Matthews, Future CO_2 Emissions and Climate Change from Existing Energy Infrastructure, *Science*, 2010, **329**, 1330–1333.
3 D. M. D'Alessandro, B. Smit and J. R. Long, Carbon Dioxide Capture: Prospects for New Materials, *Angew. Chem., Int. Ed.*, 2010, **49**, 6058–6082.
4 A. M. Appel, J. E. Bercaw, A. B. Bocarsly, H. Dobbek, D. L. Dubois, M. Dupuis, J. G. Ferry, E. Fujita, R. Hille, P. J. A. Kenis, C. A. Kerfeld, R. H. Morris, C. H. F. Peden, A. R. Portis, S. W. Ragsdale, T. B. Rauchfuss, J. N. H. Reek, L. C. Seefeldt, R. K. Thauer and G. L. Waldrop, Opportunities, and Challenges in Biochemical and Chemical Catalysis of CO_2 Fixation, *Chem. Rev.*, 2013, **113**, 6621–6658.
5 X. Chang, T. Wang and J. Gong, CO_2 Photo-Reduction: Insights into CO_2 Activation and Reaction on Surfaces of Photocatalysts, *Energy Environ. Sci.*, 2016, **9**, 2177–2196.
6 H. J. Zhu, M. Lu, Y. R. Wang, S. J. Yao, M. Kan, Y. H. Zhang, J. Liu, Y. Chen, S. L. Li and Y. Q. Lan, Efficient Electron Transmission in Covalent Organic Framework Nanosheets for Highly Active Electrocatalytic Carbon Dioxide Reduction, *Nat. Commun.*, 2020, **11**, 497.
7 J. Albero, Y. Peng and H. García, Photocatalytic CO_2 Reduction to C2+ Products, *ACS Catal.*, 2020, **10**, 5734–5749.
8 S. Barman, A. Singh, F. A. Rahimi and T. K. Maji, Metal-Free Catalysis: A Redox-Active Donor–acceptor Conjugated Microporous Polymer for Selective Visible-light-Driven CO_2 Reduction to CH_4, *J. Am. Chem. Soc.*, 2021, **143**, 16284–16292.
9 S. Biswas, A. Dey, F. A. Rahimi, S. Barman and T. K. Maji, Metal-Free Highly Stable and Crystalline Covalent Organic Nanosheet for Visible-light-driven Selective Solar Fuel

Production in Aqueous Medium, *ACS Catal.*, 2023, **13**, 5926–5937.

10 J. Qiao, Y. Liu, F. Hong and J. Zhang, A Review of Catalysts for the Electroreduction of Carbon Dioxide to Produce Low-Carbon Fuels, *Chem. Soc. Rev.*, 2014, **43**, 631–675.

11 C. Cometto, R. Kuriki, L. Chen, K. Maeda, T.-C. Lau, O. Ishitani and M. Robert, A carbon Nitride/Fe Quaterpyridine Catalytic System for Photostimulated CO_2-to-CO Conversion with Visible Light, *J. Am. Chem. Soc.*, 2018, **140**, 7437–7440.

12 X. Chen and S. S. Mao, Titanium Dioxide Nanomaterials: Synthesis, Properties, Modifications, and Applications, *Chem. Rev.*, 2007, **107**, 2891–2959.

13 S. Chen, Y. Hu, S. Meng and X. Fu, Study on the Separation Mechanisms of Photogenerated Electrons and Holes for Composite Photocatalysts g-C_3N_4-WO_3, *Appl. Catal., B*, 2014, **150–151**, 564–573.

14 Y. Zhou, Y. Zhang, M. Lin, J. Long, Z. Zhang, H. Lin, J. C. Wu and X. Wang, Monolayered Bi_2WO_6 Nanosheets Mimicking Heterojunction Interface with Open Surfaces for Photocatalysis, *Nat. Commun.*, 2015, **6**, 8340.

15 L. Cheng, Q. J. Xiang, Y. L. Liao and H. W. Zhang, CdS-based Photocatalysts, *Energy Environ. Sci.*, 2018, **11**, 1362–1391.

16 E. García-López, G. Marcì, F. R. Pomilla, M. C. Paganini, C. Gionco, E. Giamello and L. Palmisano, ZrO_2 Based Materials as Photocatalysts for 2-propanol Oxidation by Using UV and Solar Light Irradiation and Tests for CO_2 Reduction, *Catal. Today*, 2018, **313**, 100–105.

17 H. Yang, J. Tang, Y. Luo, X. Zhan, Z. Liang, L. Jiang, H. Hou and W. Yang, MOFs-derived fusiform In_2O_3 mesoporous nanorods anchored with ultrafine CdZnS nanoparticles for boosting visible-Light photocatalytic hydrogen evolution, *Small*, 2021, **17**, 2102307.

18 S. C. Yan, S. X. Ouyang, J. Gao, M. Yang, J. Y. Feng, X. X. Fan, L. J. Wan, Z. S. Li, J. H. Ye, Y. Zhou and Z. G. Zou, A Room-Temperature Reactive-template Route to Mesoporous $ZnGa_2O_4$ with Improved Photocatalytic Activity in Reduction of CO_2, *Angew. Chem., Int. Ed.*, 2010, **49**, 6400–6404.

19 J. Wang, S. Lin, N. Tian, T. Ma, Y. Zhang and H. Huang, Nanostructured Metal Sulfides: Classification, Modification Strategy, and Solar-Driven CO_2 Reduction Application, *Adv. Funct. Mater.*, 2021, **31**, 2008008.

20 S.-P. Qi, R.-T. Guo, Z.-X. Bi, Z.-R. Zhang, C.-F. Li and W.-G. Pan, Recent Progress of Covalent Organic Frameworks-based Materials in Photocatalytic Applications: A Review, *Small*, 2023, **19**, 2303632.

21 X. Feng, X. S. Ding and D. L. Jiang, Covalent Organic Frameworks, *Chem. Soc. Rev.*, 2012, **41**, 6010–6022.

22 P. J. Waller, F. Gándara and O. M. Yaghi, Chemistry of Covalent Organic Frameworks, *Acc. Chem. Res.*, 2015, **48**, 3053–3063.

23 H. Wang, H. Wang, Z. Wang, L. Tang, G. Zeng, P. Xu, M. Chen, T. Xiong, C. Zhou, X. Li, D. Huang, Y. Zhu, Z. Wang and J. Tang, Covalent Organic Framework Photocatalysts: Structures and Applications, *Chem. Soc. Rev.*, 2020, **49**, 4135–4165.

24 H. Furukawa, K. E. Cordova, M. O'Keeffe and O. M. Yaghi, Chemistry and Applications of Metal-organic Frameworks, *Science*, 2013, **341**, 1230444.

25 H. C. Zhou and S. Kitagawa, Metal-organic Frameworks (MOFs), *Chem. Soc. Rev.*, 2014, **43**, 5415.

26 Q. Wang and D. Astruc, State of the Art and Prospects in Metal–organic Framework (MOF)-based and MOF-derived Nanocatalysis, *Chem. Rev.*, 2020, **120**, 1438–1511.

27 H. Guo, D.-H. Si, H.-J. Zhu, Z.-A. Chen, R. Cao and Y.-B. Huang, Boosting CO_2 Electroreduction over a Covalent Organic Framework in the Presence of Oxygen, *Angew. Chem., Int. Ed.*, 2024, **63**, e202319472.

28 Q. J. Wu, D. H. Si, Q. Wu, Y. L. Dong, R. Cao and Y. B. Huang, Boosting Electroreduction of CO_2 over Cationic Covalent Organic Frameworks: Hydrogen Bonding Effects of Halogen Ions, *Angew. Chem., Int. Ed.*, 2023, **62**, e202215687.

29 R. Xu, D.-H. Si, S.-S. Zhao, Q.-J. Wu, X.-S. Wang, T.-F. Liu, H. Zhao, R. Cao and Y.-B. Huang, Tandem Photocatalysis of CO2 to C_2H_4 via a Synergistic Rhenium-(I)Bipyridine/Copper-Porphyrinic Triazine Framework, *J. Am. Chem. Soc.*, 2023, **145**, 8261–8270.

30 S. Navalon, A. Dhakshinamoorthy, M. Alvaro, B. Ferrer and H. Garcia, Metal-organic Frameworks as Photocatalysts for Solar-driven Overall Water Splitting, *Chem. Rev.*, 2023, **123**, 445–490.

31 Q. Wang, Q. Gao, A. M. Al-Enizi, A. Nafady and S. Ma, Recent Advances in MOF-based Photocatalysis: Environmental Remediation Under Visible Light, *Inorg. Chem. Front.*, 2020, **7**, 300–339.

32 S. Lin, S. D. Christian, Y. B. Zhang, N. Kornienko, E. M. Nichols, Y. B. Zhao, A. R. Paris, D. Kim, P. D. Yang, O. M. Yaghi and C. J. Chang, Covalent Organic Frameworks Comprising Cobalt Porphyrins for Catalytic CO_2 Reduction in Water, *Science*, 2015, **349**, 1208–1213.

33 D. Yadav, A. Kumar, J. Y. Kim, N.-J. Park and J.-O. Baeg, Interfacially Synthesized 2D COF Thin Film Photocatalyst: Efficient Photocatalyst for Solar Formic Acid Production from CO_2 and Fine Chemical Synthesis, *J. Mater. Chem. A*, 2021, **9**, 9573–9580.

34 K. Lei, D. Wang, L. Ye, M. Kou, Y. Deng, Z. Ma, L. Wang and Y. Kong, A Metal-free Donor–acceptor Covalent Organic Framework Photocatalyst for Visible-light-driven Reduction of CO_2 with H_2O, *ChemSusChem*, 2020, **13**, 1725–1729.

35 J.-X. Cui, L.-J. Wang, L. Feng, B. Meng, Z.-Y. Zhou, Z.-M. Su, K. Wang and S. Liu, A Metal-free Covalent Organic Framework as a Photocatalyst for CO_2 Reduction at Low CO_2 Concentration in a Gas–solid system, *J. Mater. Chem. A*, 2021, **9**, 24895–24902.

36 Y. Fu, X. Zhu, L. Huang, X. Zhang, F. Zhang and W. Zhu, Azine-based Covalent Organic Frameworks as Metal-free Visible Light Photocatalysts for CO_2 Reduction with H_2O, *Appl. Catal., B*, 2018, **239**, 46–51.

37 Z. Fu, X. Wang, A. M. Gardner, X. Wang, S. Y. Chong, G. Neri, A. J. Cowan, L. Liu, X. Li, A. Vogel, R. Clowes, M. Bilton, L. Chen, R. S. Sprick and A. I. Cooper, A Stable Covalent Organic Framework for Photocatalytic Carbon Dioxide Reduction, *Chem. Sci.*, 2020, **11**, 543–550.

38 W. Liu, X. Li, C. Wang, H. Pan, W. Liu, K. Wang, Q. Zeng, R. Wang and J. Jiang, A Scalable General Synthetic Approach toward Ultrathin Imine-linked Two-dimensional Covalent Organic Framework Nanosheets for Photocatalytic CO_2 Reduction, *J. Am. Chem. Soc.*, 2019, **141**, 17431–17440.

39 L. Peng, S. Chang, Z. Liu, Y. Fu, R. Ma, X. Lu, F. Zhang, W. Zhu, L. Kong and M. Fan, Visible-light-driven Photocatalytic CO_2 Reduction Over Ketoenamine-based Covalent Organic Frameworks: Role of the Host Functional Groups, *Catal. Sci. Technol.*, 2021, **11**, 1717–1724.

40 A. Dey, J. Pradhan, S. Biswas, F. A. Rahimi, K. Biswas and T. K. Maji, COF-Topological Quantum Material Nano-heterostructure for CO_2 to Syngas Production under Visible Light, *Angew. Chem., Int. Ed.*, 2024, **63**, e202315596.

41 M. Lu, M. Zhang, J. Liu, Y. Chen, J.-P. Liao, M.-Y. Yang, Y.-P. Cai, S.-L. Li and Y.-Q. Lan, Covalent Organic Framework Based Functional Materials: Important Catalysts for Efficient CO_2 Utilization, *Angew. Chem., Int. Ed.*, 2022, **61**, e202200003.

42 H. L. Nguyen and A. Alzamly, Covalent Organic Frameworks as Emerging Platforms for CO_2 Photoreduction, *ACS Catal.*, 2021, **11**, 9809–9824.

43 S. Yang, W. Hu, X. Zhang, P. He, B. Pattengale, C. Liu, M. Cendejas, I. Hermans, X. Zhang, J. Zhang and J. Huang, 2D Covalent Organic Frameworks as Intrinsic Photocatalysts for Visible Light-driven CO_2 Reduction, *J. Am. Chem. Soc.*, 2018, **140**, 14614–14618.

44 L.-j. Wang, R.-l. Wang, X. Zhang, J.-l. Mu, Z.-y. Zhou and Z.-m. Su, Improved Photoreduction of CO_2 with Water by Tuning the Valence Band of Covalent Organic Frameworks, *ChemSusChem*, 2020, **13**, 2973–2980.

45 A. Dey, F. A. Rahimi, S. Barman, A. Hazra and T. K. Maji, Metal Free 3D Donor-acceptor COF with Low Exciton Binding for Solar Fuel Production Based on CO_2 Reduction, *J. Mater. Chem. A*, 2023, **11**, 13615–13622.

46 T. Sergeieva, M. Bilichenko, S. Holodnyak, Y. V. Monaykina, S. I. Okovytyy, S. I. Kovalenko, E. Voronkov and J. Leszczynski, Origin of Substituent Effect on Tautomeric Behavior of 1,2,4-triazole Derivatives: Combined Spectroscopic and Theoretical Study, *J. Phys. Chem. A*, 2016, **120**, 10116–10122.

47 M. M. Matin, P. Matin, M. R. Rahman, T. Ben Hadda, F. A. Almalki, S. Mahmud, M. M. Ghoneim, M. Alruwaily and S. Alshehri, Triazoles and Their Derivatives: Chemistry, Synthesis, and Therapeutic Applications, *Front. Mol. Biosci.*, 2022, **9**, 864286.

48 K. T. Potts, The Chemistry of 1,2,4-triazoles, *Chem. Rev.*, 1961, **61**, 87–127.

49 A. C. Jakowetz, T. F. Hinrichsen, L. Ascherl, T. Sick, M. Calik, F. Auras, D. D. Medina, R. H. Friend, A. Rao and T. Bein, Excited-State Dynamics in Fully Conjugated 2D Covalent Organic Frameworks, *J. Am. Chem. Soc.*, 2019, **141**, 11565–11571.

50 S. Yang, D. Streater, C. Fiankor, J. Zhang and J. Huang, Conjugation-and Aggregation-Directed Design of Covalent Organic Frameworks as White-Light-Emitting Diode, *J. Am. Chem. Soc.*, 2021, **143**, 1061–1068.

51 W. Helweh, N. C. Flanders, S. Wang, B. T. Phelan, P. Kim, M. J. Strauss, R. L. Li, M. S. Kelley, M. S. Kirschner and D. O. Edwards, Layered Structures of Assembled Imine-linked Macrocycles and Two-dimensional Covalent Organic Frameworks Give Rise to Prolonged Exciton Lifetimes, *J. Mater. Chem. C*, 2022, **10**, 3015–3026.

52 R. Guntermann, L. Frey, A. Biewald, A. Hartschuh, T. Clark, T. Bein and D. D. Medina, Regioisomerism in Thienothiophene-Based Covalent Organic Frameworks– A Tool for Band-Gap Engineering, *J. Am. Chem. Soc.*, 2024, **146**, 15869–15878.

53 P. Verma, F. A. Rahimi, D. Samanta, A. Kundu, J. Dasgupta and T. K. Maji, Visible-light-driven Photocatalytic CO_2 Reduction to CO/CH_4 Using a metal–organic "Soft" Coordination Polymer Gel, *Angew. Chem., Int. Ed.*, 2022, **61**, e202116094.

54 G. Sahara and O. Ishitani, Efficient Photocatalysts for CO_2 Reduction, *Inorg. Chem.*, 2015, **54**, 5096–5104.

55 Y. Kuramochi, O. Ishitani and H. Ishida, Reaction Mechanisms of Catalytic Photochemical CO_2 Reduction Using Re(I) and Ru(II) Complexes, *Coord. Chem. Rev.*, 2018, **373**, 333–356.

56 T. J. Whittemore, C. Xue, J. Huang, J. C. Gallucci and C. Turro, Single-chromophore Single-molecule Photocatalyst for the Production of Dihydrogen Using Low-energy Light, *Nat. Chem.*, 2020, **12**, 180–185.

57 P. Roy, W. R. Browne, B. L. Feringa and S. R. Meech, Ultrafast Motion in a Third Generation Photomolecular Motor, *Nat. Commun.*, 2023, **14**, 1253.

58 R. Ghosh, A. Kushwaha and D. Das, Conformational Control of Ultrafast Molecular Rotor Property: Tuning Viscosity Sensing Efficiency by Twist Angle Variation, *J. Phys. Chem. B*, 2017, **121**, 8786–8794.

59 T. Feng, D. Streater, B. Sun, K. Duisenova, D. Wang, Y. Liu, J. Huang and J. Zhang, Tuning Photoexcited Charge Transfer in Imine-Linked Two dimensional covalent organic frameworks, *J. Phys. Chem. Lett.*, 2022, **13**, 1398–1405.

60 X. Li, Y. Sun, J. Xu, Y. Shao, J. Wu, X. Xu, Y. Pan, H. Ju, J. Zhu and Y. Xie, Selective Visible-light-driven Photocatalytic CO_2 Reduction to CH_4 Mediated by Atomically Thin $CuIn_5S_8$ Layers, *Nat. Energy*, 2019, **4**, 690–699.

61 R. Zhang, H. Wang, S. Tang, C. Liu, F. Dong, H. Yue and B. Liang, Photocatalytic Oxidative Dehydrogenation of Ethane Using CO_2 as a Soft Oxidant Over Pd/TiO_2 Catalysts to C_2H_4 and Syngas, *ACS Catal.*, 2018, **8**, 9280–9286.

62 Q. Li, H. Yue, C. Liu, K. Ma, S. Zhong, B. Liang and S. Tang, A Photocatalytic Transformation Realized by Pd/TiO_2 Particle Size Modulation: From Oxidative Dehydrogenation of Ethane to Direct Dehydrogenation of Ethane, *Chem. Eng. J.*, 2020, **395**, 125120.

63 F. A. Rahimi, S. Dey, P. Verma and T. K. Maji, Photocatalytic CO_2 Reduction Based on a Re(I)-Integrated Conjugated Microporous Polymer: Role of a Sacrificial Electron Donor in Product Selectivity and Efficiency, *ACS Catal.*, 2023, **13**, 5969–5978.

64 D. Ren, J. Fong and B. S. Yeo, The Effects of Currents and Potentials on the Selectivities of Copper toward Carbon dioxide Electroreduction, *Nat. Commun.*, 2018, **9**, 925.